

# Energy optimization of synchrotron microCT for high-throughput phenotyping of zebrafish

Alexandra Rojek

Department of Radiology, The University of Chicago

August 20, 2010

## Abstract

In the study of human development and abnormal gene function, model organisms must be used in order to better understand complex gene functions and diseases. Zebrafish are an important biological vertebrate model of the human system, which are intriguing for genetic screening. The ultimate goal is to establish a zebrafish atlas to document normal zebrafish anatomy in order to compare them to mutant zebrafish. In order to accomplish this goal, microCT at a synchrotron is used to allow for 3D imaging as well as high resolution of images. The goal of this study is to optimize the energy selection in three different cases: single-energy, dual-energy, and triple-energy. The single-energy case is based on optimizing the contrast-to-noise ratio, and analysis showed that although the maximum CNR occurred at relatively low energy values, this peak value can be shifted by adjusting other measurements. The dual-energy case evaluated whether imaging at absorption edges resulted in the least variance in an image, and surprisingly, it was found that this was not always the case. In the triple-energy case, the results largely supported and expanded on those of the dual-energy case and left room for further analysis of what this means in terms of applications for future scanning. The results found by this study aid in the determination of which energies to scan in order to optimize variance, and have future applications in not only synchrotron microCT, but also emerging technologies such as photon-counting detector systems.

# 1 Introduction

In the study of human development and abnormal gene function, model organisms must be used in order to better understand complex gene functions and diseases. Zebrafish are an important biological vertebrate model of the human system, which are intriguing for genetic screening, as seen in Lamason *et al.*[3]. Their applicability spans studies of development, organogenesis, neurobiology, cancer biology, and toxicology. The zebrafish is appropriate for cancer studies, as it has been shown that it is an applicable model to specific cancers, such as skin cancer, as seen through the discovery of the gene which regulates melanocyte and therefore melanin production [3]. It is also a convenient organism because of its transparent, externally fertilized embryos, as well as its rapid development. In an effort by the Cheng lab at Penn State to establish an atlas focused on 2D histology, the goal is to document normal zebrafish anatomy in order to compare them to mutant zebrafish. 2D histology is limiting, however, in quantitative structural analysis and as such, microCT has emerged as a viable 3D imaging option [4].

Computed tomography (CT) scanning functions by creating a tomographic image of the subject by passing X-rays through the subject and measuring their absorption from a variety of angles, thereby creating an image of absorption coefficients. A standard, commercial medical CT scanner uses a polychromatic beam, or one where the energies of the X-rays are not uniform. A synchrotron source, on the other hand, is capable of using monochromatic X-ray beams, which contain photons which are at one energy. At a synchrotron source, high-speed electrons circulate in a storage ring where their trajectories are corrected for using a large electromagnet lattice. As electrons circulate in the ring, they decelerate due to the electromagnets, and thus emit an electromagnetic spectrum which consists of many types of waves, thus creating a polychromatic X-ray spectrum. However, this spectrum is so intense that it can be made into a monochromatic, or single energy, beam and still have a high enough flux, or photon count, to be useful to tomographic applications [7].

The X-rays produced from a commercial medical device or a synchrotron proceed to be passed through the subject of interest at different orientations about the subject. The transmission of the X-rays is measured by linear detector arrays which are on the opposite side of the X-ray source. From these transmissions of the X-rays, a profile of the cross section of the subject is produced. In a commercial medical scanner, the resulting reconstructed image is used to make diagnoses about pathologies present in the subject [2].

The reconstruction of an image from the transmission data is possible through the phenomenon of attenuation, or the removal of photons from the X-ray beam as it passes through the subject. Attenuation is comprised of absorption and scattering of the photons as they pass through a given material. At different energies, the attenuation effects are dominated by different process: the photoelectric effect, Compton effect,

and pair production. Attenuation is dependent on the linear attenuation coefficient, which is the fraction of photons removed from a monoenergetic X-ray beam per unit of thickness of the material, and is expressed in  $\text{cm}^{-1}$ . The linear attenuation coefficient is the sum of all the attenuations of the different effects described above for a certain material at a given energy [2].

The concept of the linear attenuation coefficient, when normalized to unit density, is called the mass attenuation coefficient, with units of  $\text{cm}^2/\text{g}$ . It is important to note, however, that mass attenuation is independent of density, and only normalizes for it. The Beer-Lambert Law is modified to be expressed in the form where  $\mu/\rho$  is the mass attenuation coefficient,  $\rho$  is density,  $l$  is length,  $I_0$  is the original intensity of the beam, and  $\bar{I}$  is the intensity of the beam transmitted.

$$\bar{I} = I_0 e^{-(\mu/\rho)\rho l}$$

In general, the attenuation of a given material decreases as a function of increasing energies of the X-ray beam. The exception to this rule is at absorption edges, or K-edges and L-edges. These edges are created by the photoelectric effect on the attenuation of X-rays.

In the photoelectric effect, the incident photon energy is transferred to an electron in the given atom, which is then emitted as a photoelectron. In order for this photoelectron to be ejected, the energy of the incident photon must be greater than or equal to the binding energy of the electron in the atom which is to be emitted. The electron(s) closest to the incident photon energy, but also with binding energies less than the incident photon energy, are most likely to be emitted. As this photoelectron is emitted, the atom is ionized as it has an inner-shell electron vacancy. The electrons from outer shells cascade down to fill in the vacancy in the shell of the photoelectron, thus emitting characteristic X-rays. The probability of the photoelectric effect occurring is described as  $\frac{Z^3}{E^3}$  where  $Z$  is the atomic number of the atom and  $E$  is the energy of the incident photon. For a given energy, this shows that an element with a higher atomic number has a much higher probability of photoelectric interaction, as there are more shells of electrons which can undergo this process[2].

For incident photon energies close to a given ionization binding energy, an incident photon energy just below this threshold will not ionize the atom and photoelectric absorption will not occur. When the incident photon reaches the appropriate energy, there is a sudden jump in the absorption of X-rays in the atom as the incident photon is now able to overcome the binding energy and cause the release of a photoelectron. This creates the jump in absorption known as the K-edge or L-edge (depending on which shell the electron is originally in)[2].

Absorption edges are specific to the type of element being used. For example, an element with a low atomic number does not have many edges since it has fewer electrons, meaning fewer shells, which in turn means no absorption edges at different shells. Other elements, with higher atomic number have more electrons, along

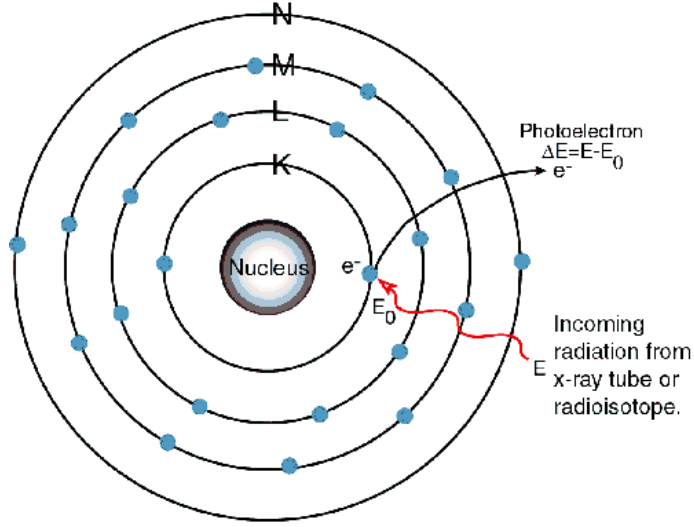


Figure 1: Illustration of the photoelectric effect on an atom, with a photoelectron being emitted[7].

with more shells, which presents the opportunity for more absorption edges, especially at lower energies, and therefore allowing the element to be more practically useful [5].

Absorption edges can be used in digital subtraction imaging with the use of synchrotron wavelength-tunability. This technique uses the fact that most bodily tissues are made up of light elements (oxygen, carbon, hydrogen) which do not have corresponding absorption edges at the energies which the contrast agents do. Using this knowledge, if an image containing a high-Z element is imaged right above and below the absorption edge, then a digital subtraction of the pixel values in both images results in an image of only the regions where high-Z element stains the specimen. This is possible because the attenuation in the tissue materials does not change appreciably over such a small pairing of energies, while the attenuation of the contrast element changes considerably due to the absorption edge (seen in Figure 2).

The application of this kind of imaging technique would have the potential to not only aid in the imaging of model organisms for genetic comparison, but also in the diagnosis of cancers in both model organisms and humans, with the aid of future technological developments. With the discovery of a contrast agent which would selectively stain tumors, this kind of subtraction imaging would be extremely useful in localizing tumors and diagnosing cancers. More precise imaging of these types of diseases could reduce the prevalence of artifacts, and have the ability to possibly detect metastases earlier, and therefore increase treatment prognosis.

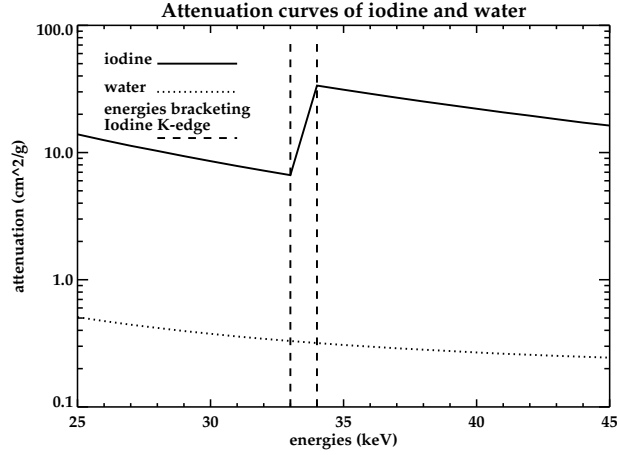


Figure 2: At 33.169 keV, iodine has a K-edge at which the attenuation significantly changes, while the attenuation of water has negligible change as compared to that of iodine. Imaging right above and below the iodine K-edge (33 and 34 keV) would allow digital subtraction to be used to obtain an image of only the iodine.

## 2 Methods

### 2.1 Energy optimization for single-energy studies

When scanning a specimen with only one energy, our goal is to maximize the difference between the contrast material (a high-Z, heavy metal stain) and the background material (matrix), while also minimizing the noise. This can be quantitatively analyzed by the contrast-to-noise ratio (CNR). The model which this analysis assumes is a circular matrix material of diameter  $D_m$  with a circular contrast agent of diameter  $D_c$  placed in the center of the matrix material. This set-up can be seen in Figure 3. The energy-dependent attenuation coefficient of the matrix material can then be defined as  $\mu_m(E)$  and that of the contrast agent can be defined as  $\mu_c(E)$ . The contrast of the image can be defined as  $|\mu_c(E) - \mu_m(E)|$ .

The transmitted intensity of the beam can also be defined as

$$\bar{I}(E) = I_0(E) \exp \{ -\mu_c(E)D_c - \mu_m(E)D_m \},$$

The variance in the estimate of the contrast agent is given by

$$\sigma_{\mu_c}^2 \propto \frac{1}{\bar{I}(E)}.$$

The standard deviation can then be defined as

$$\sigma_{\mu_c} \propto \frac{1}{\sqrt{\bar{I}(E)}}.$$

Our goal is to then maximize the CNR, which can be defined as

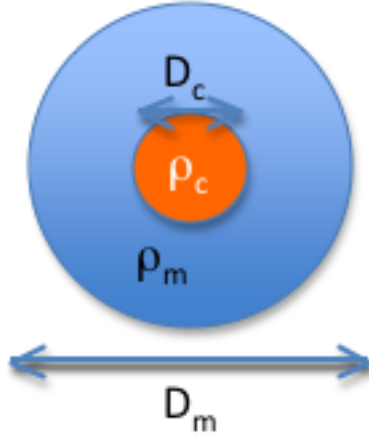


Figure 3: Visualization of the set-up for the CNR study[4].

$$CNR = \frac{|\mu_c(E) - \mu_m(E)|}{\sigma_{\mu_c}}.$$

From this equation, the standard deviation can be replaced with an equation from above, yielding

$$CNR = |\mu_c(E) - \mu_m(E)| \sqrt{\bar{I}(E)}$$

And substituting in the equation for transmittance leaves us with

$$CNR = \sqrt{\bar{I}(E)} |\mu_c(E) - \mu_m(E)| \sqrt{\exp\{-\mu_c(E)D_c - \mu_m(E)D_m\}}$$

In order to analyze the optimal energies using this method of analysis, energies ranging from 1 to 100 keV were analyzed in 1 keV increments, with the units of CNR being arbitrary. In order to analyze the changes in optimal energies, different densities and total matrix lengths were used to determine the changes in optimal CNR values. According to an average value of density determined from scans of zebrafish at Argonne National Laboratory Advanced Photon Source, it was found that the density of the contrast agent was approximately 0.0005 g/cc. Due to this, the effect of different densities within an order of magnitude of 0.0005 g/cc (or 0.00005 to 0.005 g/cc) was analyzed. Different total lengths of the matrix material were also analyzed, ranging from 1 mm to 5 mm total, while keeping the length of the contrast agent constant at 0.1 mm.

## 2.2 Energy optimization for multiple-energy studies

When considering dual-energy scanning with micro-CT, our goal is to be able to optimize the contrast between the contrast agent and the background material, while also minimizing the noise of the image. It was previously thought that the best method to accomplish this goal would be to image right above

and below the absorption edge of the heavy element contrast agent, and subsequently use absorption-edge digital subtraction, as described above. However, in order to analyze whether this is the best method for accomplishing this goal, the Fisher information matrix and the Cramer-Rao lower bound were used.

In estimation theory, the Cramer-Rao lower bound (CRLB) states that the variance of an unbiased estimator cannot be lower than the inverse of the Fisher information matrix, which is the covariance matrix of the log-likelihood of a data vector. Outside of theory, this lower bound can be achieved with an efficient estimator. This type of estimator must be unbiased, meaning that the difference between the estimator's expected value and the true value of the parameter being estimated must be zero (the densities of the elements are the true values of the image). Such an unbiased estimator which achieves this lower bound (which is what we seek to do) is said to be an efficient estimator.

Considering illumination  $I_0(E)$ , the measurement of  $I(E)$  can be given by

$$\bar{I}(E) = I_0(E) \exp \left\{ - \sum_{i=1}^N \left[ \frac{\mu}{\rho}(E) \right]_i \rho_i \tau_i \right\}.$$

We define  $a_i^{(j)} \equiv \left[ \frac{\mu}{\rho}(E) \right]_i$ ,  $\bar{I}^{(j)} \equiv \bar{I}(E_j)$ ,  $I_0^{(j)} \equiv I_0(E_j)$ , and  $x_i \equiv \rho_i \tau_i$  where  $N$  is the number of materials involved in the analysis and  $i$  is a given material. Then rewriting the above equation leaves us with,

$$\bar{I}^{(j)} = I_0^{(j)} e^{-\sum_{i=1}^N a_i^{(j)} x_i}.$$

We define  $\mathbf{x} = [x_1, \dots, x_N]$  to be the set of  $x_i$ , or a vector of the densities present in the image, for the  $N$  different materials present.

In reality, we assume the actual measurements are Poisson random variables  $I^{(j)}$  having mean  $\bar{I}^{(j)}$  and probability distribution

$$p(I^{(j)} | \mathbf{x}) = \frac{e^{-\bar{I}^{(j)}} (\bar{I}^{(j)})^{I^{(j)}}}{\bar{I}^{(j)}!}.$$

Consider a vector of measurements acquired at  $M$  different energies:  $\mathbf{I} = [I^{(1)}, \dots, I^{(M)}]$ . Then the joint probability of acquiring that set of measurements is given by

$$p(\mathbf{I} | \mathbf{x}) = \prod_{j=1}^M \frac{e^{-\bar{I}^{(j)}} (\bar{I}^{(j)})^{I^{(j)}}}{\bar{I}^{(j)}!}.$$

The log-likelihood is then given by

$$L(\mathbf{x}) \equiv \ln p(\mathbf{I} | \mathbf{x}) = \sum_{j=1}^M \left\{ -\bar{I}^{(j)}(\mathbf{x}) + I^{(j)} \ln \bar{I}^{(j)}(\mathbf{x}) \right\},$$

where we have made the dependence of  $\bar{I}^{(j)}(\mathbf{x})$  on  $\mathbf{x}$  and omitted a term that does not depend on  $\mathbf{x}$ , as we are looking for the maximum of  $L(\mathbf{x})$  with respect to  $\mathbf{x}$ .

The Fisher information matrix  $F$  has elements  $F_{mn}$  equal to

$$F_{mn} = E \left\{ - \frac{\partial^2 L}{\partial x_m \partial x_n} \right\},$$



where  $E\{\}$  denotes the expectation value.

Through the use of partial derivatives,

$$\frac{\partial^2 L}{\partial x_m \partial x_n} = \frac{\partial}{\partial x_m} \left[ \frac{\partial L}{\partial x_n} \right]$$

To first find the partial derivative of the log likelihood function with respect to  $\chi_n$  (density times length),

$$\frac{\partial L}{\partial x_n} = \frac{\partial}{\partial x_n} \left[ \sum_j \left\{ I^{(j)} \ln \bar{I}^{(j)}(\mathbf{x}) - \bar{I}^{(j)}(\mathbf{x}) \right\} \right],$$

$$\frac{\partial L}{\partial x_n} = \sum \left\{ I^{(j)} \frac{\partial}{\partial x_n} \ln \bar{I}^{(j)}(\mathbf{x}) - \frac{\partial}{\partial x_n} \bar{I}^{(j)}(\mathbf{x}) \right\},$$

$$\frac{\partial L}{\partial x_n} = \sum \left\{ I^{(j)} \frac{1}{\bar{I}^{(j)}(\mathbf{x})} \frac{\partial}{\partial x_n} \bar{I}^{(j)}(\mathbf{x}) - \frac{\partial}{\partial x_n} \bar{I}^{(j)}(\mathbf{x}) \right\},$$

$$\frac{\partial L}{\partial x_n} = \sum \left\{ \left[ \frac{I^{(j)}}{\bar{I}^{(j)}(\mathbf{x})} - 1 \right] \frac{\partial}{\partial x_n} \bar{I}^{(j)}(\mathbf{x}) \right\},$$

Consequently, in order to find the partial derivative of  $\bar{I}^{(j)}(\mathbf{x})$  then,

$$\frac{\partial}{\partial x_n} \bar{I}^{(j)}(\mathbf{x}) = I_0^{(j)} e^{-\sum_{i=1}^N a_i^{(j)} x_i} \left[ \frac{\partial}{\partial x_n} \left\{ -\sum_i a_i^{(j)} x_i \right\} \right],$$

and by substituting in  $\bar{I}^{(j)}(\mathbf{x})$  and distributing the derivative, we have

$$\frac{\partial}{\partial x_n} \bar{I}^{(j)}(\mathbf{x}) = \bar{I}^{(j)}(\mathbf{x}) \left[ -\sum_i a_i^{(j)} \frac{\partial x_i}{\partial x_n} \right].$$

Now,  $\frac{\partial x_i}{\partial x_n} = \delta_{in}$  where  $\delta_{in}$  is the Kronecker delta, which equals 1 when  $i = n$ , and 0 otherwise. So only one term in the sum is non-zero,

$$\frac{\partial}{\partial x_n} \bar{I}^{(j)}(\mathbf{x}) = \bar{I}^{(j)}(\mathbf{x}) \left[ -a_n^{(j)} \right]$$

Substituting this partial derivative back into the original derivation leaves us with,

$$\frac{\partial L}{\partial x_n} = \sum_j \left[ \frac{I^{(j)}}{\bar{I}^{(j)}(\mathbf{x})} - 1 \right] \bar{I}^{(j)}(\mathbf{x}) (-a_n^{(j)})$$

$$\frac{\partial L}{\partial x_n} = \sum_j \left[ I^{(j)} - \bar{I}^{(j)}(\mathbf{x}) \right] a_n^{(j)}$$

Now, placing the partial derivative of the log likelihood function back into the second partial derivation of the log likelihood function leaves,

$$\frac{\partial^2 L}{\partial x_m \partial x_n} = \frac{\partial}{\partial x_m} \left[ - \sum_j \left\{ I^{(j)} a_n^{(j)} - \bar{I}^{(j)}(\mathbf{x}) a_n^{(j)} \right\} \right]$$

Here, the term  $I^{(j)} a_n^{(j)}$  can be removed, as it does not deal with the vector  $\mathbf{x}$ .

$$\frac{\partial^2 L}{\partial x_m \partial x_n} = \frac{\partial}{\partial x_m} \sum_j \left[ \bar{I}^{(j)}(\mathbf{x}) a_n^{(j)} \right]$$

$$\frac{\partial^2 L}{\partial x_m \partial x_n} = \sum_j a_n^{(j)} \left[ \frac{\partial}{\partial x_m} \bar{I}^{(j)}(\mathbf{x}) \right]$$

And through our previous derivation of  $\bar{I}^{(j)}(\mathbf{x})$  we know that

$$\frac{\partial^2 L}{\partial x_m \partial x_n} = \sum_j a_n^{(j)} \left[ -\bar{I}^{(j)}(\mathbf{x}) a_m^{(j)} \right]$$

So, finally

$$\frac{\partial^2 L}{\partial x_m \partial x_n} = - \sum_j a_n^{(j)} a_m^{(j)} \bar{I}^{(j)}(\mathbf{x})$$

Now that we know the second partial derivative of the log likelihood function with respect to  $x_m$  and  $x_n$ , we can determine that the Fisher matrix element for materials  $m$  and  $n$  is

$$F_{mn} = \sum_j a_n^{(j)} a_m^{(j)} \bar{I}^{(j)}(\mathbf{x})$$

After constructing the Fisher information matrix using the above equation, the inverse is taken, resulting in the covariance matrix which is the basis of the Cramer-Rao lower bound. The elements of the inverse matrix which are of interest, namely the diagonal elements from top left to bottom right, are the CRLB values for the respective energy combination, which can then be used to analyze the optimal energies for a given specimen.

When looking at dual-energy optimization, a two-dimensional matrix is constructed with axes corresponding to the energies which are being analyzed for optimization. The members of the matrix are the CRLB values for the two energies on the corresponding axes, and of these, the one with the lowest CRLB value is chosen as the optimal energy pairing. When looking for a triple-energy optimization (when using two contrast agents simultaneously), a three-dimensional matrix is constructed and the same process is followed as for a dual energy case, with the exception that the resulting energy optimization is a set of three energies.

To analyze the theory that imaging at the absorption edge would be most efficient in a dual-energy decomposition, a test case using iodine as the contrast element and water as the matrix material was used. This test case analyzed for changes in energy pairings across different density values, while the total length

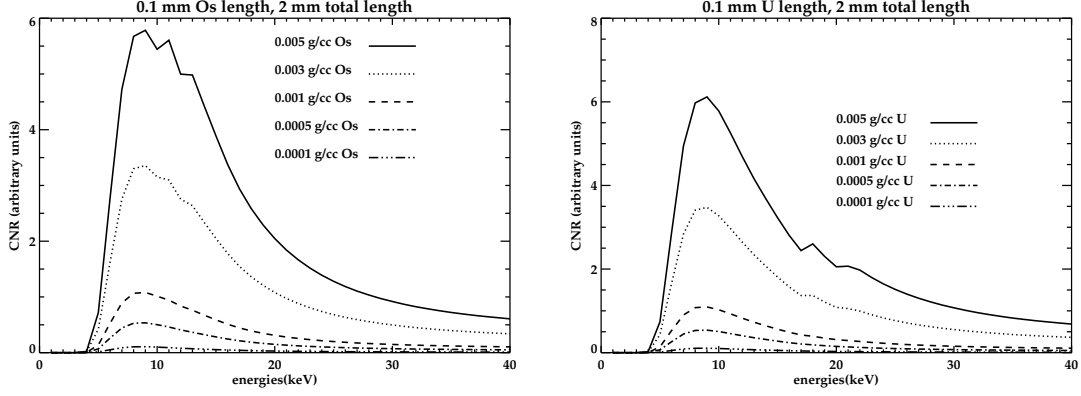


Figure 4: Analysis of the effect of contrast agent density on the relative CNR when keeping the contrast agent length constant at 0.1 mm and keeping the length of the specimen at 2 mm. It can be seen that with decreasing density, the CNR values become relatively smaller. However, the corresponding energy of the maximum value of the CNR does not change across densities. It can also be seen that the L-edges around 12 keV for Os and around 20 keV for U do have a visible effect on the CNR values .

of the specimen was held constant at 2 mm in length, the length of the constrast was held constant at 0.1 mm, and the density of the matrix material, or water, was held constant at 1 g/cc.

In order to further test this procedure for determining more than two optimal energies, the derivation above was analyzed in use for specimens containing two of the following elements in any combination: tungsten, osmium, and uranium. The matrix material was again assumed to be water, with a density of 1 g/cc and a length of 2 mm, with 0.1 mm lengths of the contrast elements.

### 3 Results

#### 3.1 Energy optimization with single-energy studies

We found that for all contrast agent elements, the effects of changing the total length of the specimen and changing the density of the contrast agent affected the calculated CNR in the same predictable pattern. As the total length of the specimen was increased, the peak value of the CNR occurred at higher energy values than when the total length was smaller. As density was changed, the energy which corresponded to the maximum CNR value did not change, although the CNR value did decrease with decreasing density values. Both of these effects can be seen in Figures 4 and 5 .

#### 3.2 Energy optimization with dual-energy studies

##### 3.2.1 Iodine contrast

For the test case of the iodine contrast in a water matrix material, the theory that imaging at the K-edge of iodine would show the least variance was confirmed for a certain range of density values, as shown in Figure 6.

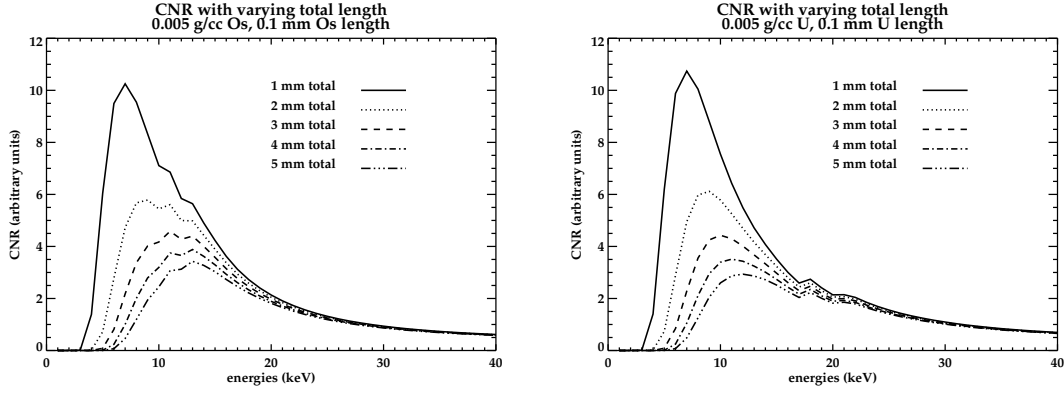


Figure 5: Here, the effects of changing the total length of the specimen while keeping the density at 0.005 g/cc and the length of the contrast agent constant at 0.1 mm can be seen. Although the CNR value does decrease as the total length of the specimen increases, the corresponding energy of the CNR peak shifts to higher energies as the total length increases. As in the figure above, the effect of the L-edges on the CNR is also visible.

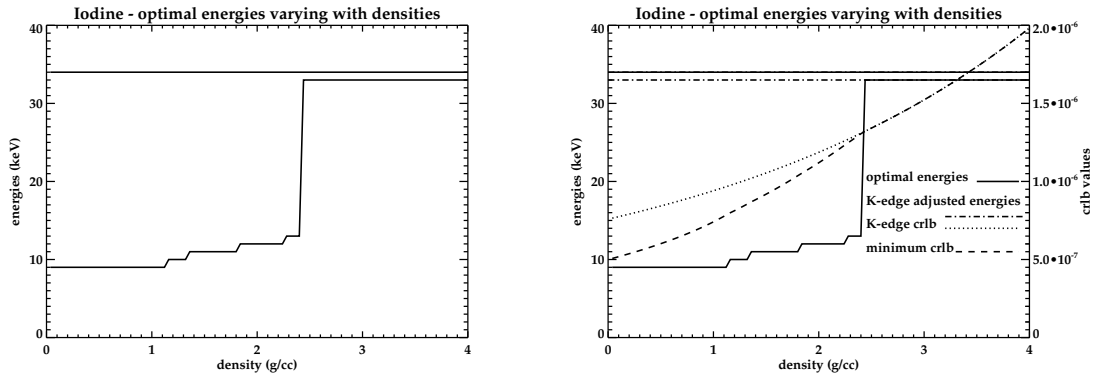


Figure 6: Optimal dual-energy pairing for iodine across a range of density values of the iodine contrast, based on the ultimate minimum of the CRLB values (left). On the right is a graph of the energy pairings which are chosen in order to bracket the K-edge, along with the difference in CRLB values between the optimal energy pairings the K-edge chosen energies. In both cases, the total length of the specimen is 2 mm and the length of the iodine contrast is 0.1 mm.

Here, it can be seen that the energies chosen by the optimization program have the lower energy of the pair placed at 9 keV, while the higher energy was positioned above the K-edge, at 34 keV. As the density value increases, the energy pairings come to exactly bracket the K-edge of iodine with an energy pair of 33 keV and 34 keV. At the lower density values, the energy pair does not bracket the K-edge because the amount of the iodine present in the sample is relatively small, and so a considerable amount of the incident beam is not being attenuated by the iodine. To avoid this problem, scanning one of the images at a lower energy allows for more incident photons to be attenuated relative to the total amount of incident photons present.

In order to evaluate whether scanning at the K-edge of iodine would be significantly worse than at the optimal energies chosen by the minimum value of the CRLB matrix, the program was modified to evaluate the trade-off in variance between optimal and K-edge energies. The results of this evaluation are also seen in Figure 6, which shows that the differences in variance are not extremely great, suggesting that it is possible to consider scanning at the K-edge even when the optimal energy pairing suggests that lower energies should be used for the decomposition.

### 3.2.2 Osmium and Uranium Contrasts

We also worked with contrast agents which have both been used in past scans at Argonne Advanced Photon Source with zebrafish, in the form of osmium tetroxide, uranyl acetate, and phosphotungstic acid. Biologically, it is expected the osmium should stain lipids in cell membranes, uranium should stain nucleic acids, and tungsten should stain fibers of connective tissue. These contrast agents were expected to produce optimal scans when bracketing their L-edges. With these contrast agents, similar results were produced as with the iodine test case, as shown in Figure 7 and 8 for osmium and uranium.

## 3.3 Energy optimization with triple-energy studies

In the triple-energy decomposition situation, there was no expectation similar to that of bracketing the K- or L-edge as in all the dual energy cases. As a result, the energy choices in a triple-energy decomposition which were discovered have elements which both confirm some preliminary preconceptions as well as offer new insight into what may be optimal for such situations.

The energy triplets which were chosen by achieving the lower bound on the variance seemed to indicate that two of the values of the energy triplet bracketed the L-edges (in Os, U, and W). The third value seems to depend on the combination of contrast agents and their relative absorption edges. In this case, if the contrast agent elements are close in atomic number, and therefore closer in L-edge values, the third energy

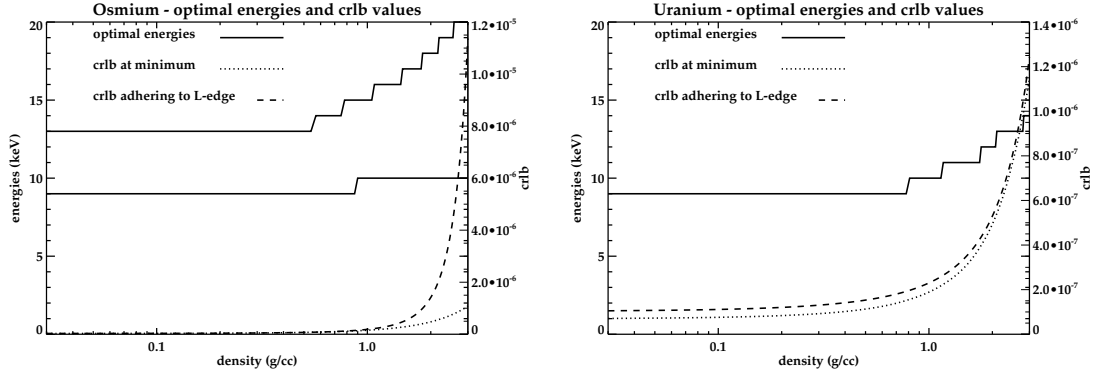


Figure 7: Shown here are the optimal energies as determined by the minimum CRLB values, as well as plots of the CRLB at those points, and in comparison to the CRLB values if energies surrounding the L-edge of each element were to be used. It can be seen that there is not a substantial difference in the variance for cases where the energies surrounding the L-edge are chosen. The total length of the specimen in these situations is 2 mm and the length of the contrast is 0.1 mm

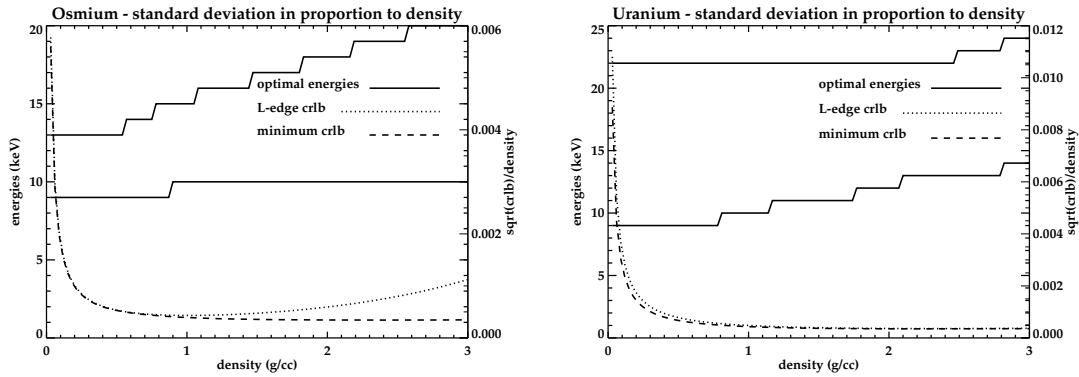


Figure 8: In this analysis of osmium and uranium, the square root of the variance, or the standard deviation, is divided by the density to analyze the proportion of the standard deviation with regards to density. Although all the values are within a reasonable range (they all fall under 1% on these graphs), the values are higher at lower densities. This is not a cause for immediate concern, as the ratio of standard deviation to density still falls within a reasonable range, and the ratios can be decreased by increasing dwell time. The total length of the specimen in these situations is 2 mm and the length of the contrast is 0.1 mm

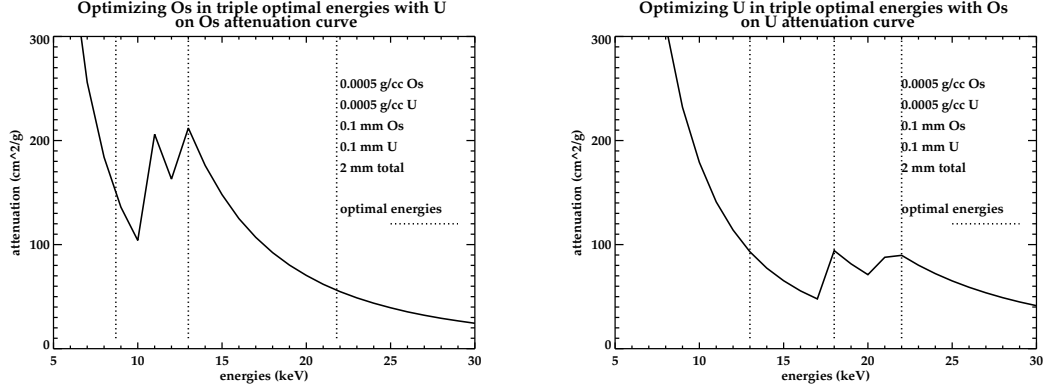


Figure 9: Here, the triple energy technique is applied to a specimen where the background material is water, and the two contrast agents are osmium and uranium, with details shown on legend of the graph. The optimal energies as shown on the graph on the left, optimize Os in a specimen where both Os and U are present, at 8.7 keV, 13.0 keV, and 21.8 keV. The energies to optimize U in the same image are shown on the graph on the right, as 13.0 keV, 18.0 keV, and 22.0 keV.

of the determined energy triplet adheres more closely to their L-edges as opposed to when the elements are farther apart in atomic number.

The optimal energy sets for different contrast elements are shown in Figures 9, 10, and 11.

## 4 Discussion

The implications of our findings both were able to shed light on past scanning techniques as well as provide insight for future optimization. In the case of optimization with a single energy, we saw that the peaks of CNR occurred at relatively low energy values, which was not highly expected, although reasonable.

The findings from the dual energy studies revealed the most in the low-density range where the K- or L-edge was not chosen to be bracketed as had been expected previously. The reasoning for initially assuming that these edges would be best for imaging are seen in Figure 4 where the attenuation of a contrast agent differs highly from the attenuation of the background material. However, as seen in the results, for low density values, the energy pairings indicated by the program did not exactly coincide with these absorption edges. On the contrary, they did tend to coincide nicely with the CNR peaks, although these two analyses were unrelated.

The reasoning for such differences in energy pairings according to the lower bound on variance is that at such low densities of these high atomic number elements, the attenuation at higher energies may be minimal, which would be why the program suggested scanning at lower energies where attenuation would be proportionally higher. This, however, presents other logistical problems, as there are other factors in

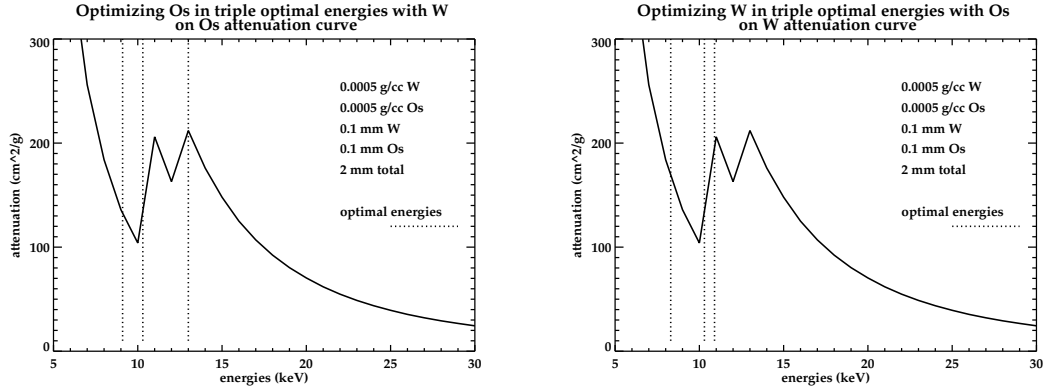


Figure 10: The triple energy technique is applied to a specimen where the background material is water, and the two contrast agents are osmium and tungsten, with details shown on legend of the graph. The optimal energies as shown on the graph on the left, optimize Os in a specimen where both Os and W are present, at 9.1 keV, 10.3 keV, and 13.0 keV. The energies to optimize W in the same image are shown on the graph on the right, as 8.3 keV, 10.3 keV, and 10.9 keV.

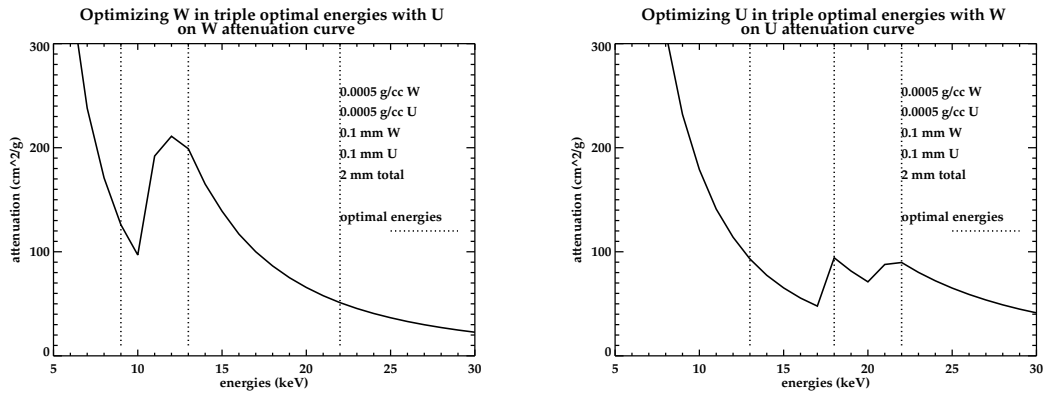


Figure 11: The triple energy technique is applied to a specimen where the background material is water, and the two contrast agents are tungsten and uranium, with details shown on legend of the graph. The optimal energies as shown on the graph on the left, optimize W in a specimen where both W and U are present, at 9.0 keV, 13.0 keV, and 22.0 keV. The energies to optimize U in the same image are shown on the graph on the right, as 13.0 keV, 18.0 keV, and 22.0 keV.



determining which energies are best to scan at in regards to limitations in technology as well as other confounding dimensionality issues.

The results of the triple energy studies both confirmed some preconceptions that we had formed based on the dual energy studies, as well as presented some new material and new ideas, which were not intuitive in nature. One of the largest issues was determining how to optimize both contrast elements at once, since the method which was used here was designed to determine the optimal energy triplet for either element. Modifying this to include both elements produced energy sets which seemed to optimize only one of the contrast agents. This presents the possibility of modifying the current technique in order to optimize both contrast agents with only one set of three energies.

These methods of monochromatic X-ray scanning of zebrafish and other model organisms present the possibility of improving microCT images so that noise is reduced by minimizing the variance. The practical application of such methods is capable of being implemented with current technologies at such sources as the Argonne National Laboratory Advanced Photon Source, where the synchrotron is able to be fine-tuned as to use the results shown in these analyses. Other possible implementations include bench-top, monochromatic CT systems which are currently being developed [6].

In the process of implementing these findings, there are some foreseeable difficulties which could occur due to some unaddressed variables. For example, the existence of bone artifacts in zebrafish samples may complicate the scanning of these specimens at lower energies as such highly attenuating materials are not accounted for in this model, where it is assumed that the specimen consists mostly of only the background matrix (water) and the contrast agent. Another confounding variable may be the presence of another matrix material, such as a resin, which is used to fix the specimen in place for scanning. It is possible, however, to adjust for these changes in the specimen material in the implementation of this theory, and to receive accordingly adjusted results for different zebrafish samples.

Although very specific in nature, these results, along with other optimizations of scanning zebrafish and other model organisms like it, present the opportunity for optimizing a type of scanning which can aid in biological analysis of different mutants and diseases like cancer, among other things. By reducing the noise of an image or optimizing the contrast-to-noise ratio, the quality of the image is much improved in that it presents more of what is actually present in the image as opposed to elements which should not be present in the image for diagnostic uses.

A long term application of this work includes using this type of theoretical application in human CT. Developments which would have to be made in order for this theory to be applicable to humans includes the development of the previously mentioned benchtop monochromatic X-ray source, or the use of a photon-counting CT system. The possible implementation of this technique has the potential yield better images

which can in turn aid in the diagnosis of such life-threatening diseases in humans as cancer.

## 5 Acknowledgments

I would like to convey immense gratitude to Dr. Patrick La Rivière for taking me on as a member of his lab for what, although now seems to be a very short eight weeks, has been one of the most incredible experiences of my life. The experience has not only taught me about something so specific yet so fascinating, but also about a scientific field that I never imagined would interest me so much. I will be forever indebted to all the time that Dr. La Rivière devoted to mentoring me this summer, through all the mistakes and questions, for altogether it has taught me not only how to conduct research, but that not all research needs to involve cells and gels to be significant and worthwhile. I would like to also thank Phillip Vargas for taking so much time away from moving his way up on the ranking of cluster space users, and to Dimple Modgil for taking time away from her photo acoustic phantoms and writing her dissertation to answer my questions every day. I would also like to thank the rest of the La Rivière lab, Kevin Little and Adam Petschke, for being supportive throughout my entire experience, and for accepting me in the lab and making me feel at home in this new environment, to the point where I did not want to leave the lab, ever. Lastly, I would like to thank the American Cancer Society for offering me with this incredible opportunity, which I could not have had the access to otherwise, and as it has been truly a life-changing experience.

## References

- [1] Attix, Frank H. Introduction to Radiological Physics and Radiation Dosimetry. Germany: Wiley-VCH Verlag GmbH & Co. KGaA, 1986.
- [2] Bushberg, Jerrold T., J A. Seibert, Edwin M. Leidholdt, Jr., and John M. Boone. Essential Physics of Medical Imaging. 2nd ed. Philadelphia: Lippincott Williams & Wilkins, 2002.
- [3] Lamason, Rebecca L., Manzoor-Ali P. Mohideen, Jason R. Mest, Andrew C. Wong, and Heather L. Norton. "SLC24A5 affects pigmentation in zebrafish and man." *Science* 310 (2005): 1782-86. Print.
- [4] La Rivière, Patrick J., Darin Clark, Alexandra Rojek, Phillip Vargas, and Xianghui Xiao. "Optimizing synchrotron micro-CT for high-throughput phenotyping of zebrafish." *Proceedings of SPIE* 7804 (2010). [in press].
- [5] Margaritondo, Giorgio. Elements of Synchrotron Light. Oxford: Oxford University Press, 2002.
- [6] Sarnelli, A, A Taibi, A Tuffanelli, G Baldazzi, and D Bollini. "K-edge digital subtraction imaging based on a dichromatic and compact x-ray source." *Physics in Medicine and Biology* 49 (2004): 3291-305. Print.
- [7] Wildenschild, D, J W. Hopmans, CMP Vaz, M L. Rivers, and D Rikard. Using X-ray computed tomography in hydrology: systems, resolutions, and limitations. *Journal of Hydrology*; 267 (2002): 285-297.
- [8] Xfr\_1.gif. University of Minnesota Methods of Experimental Physics Laboratory. Web. 9 Aug. 2010.